Supporting Information

Y-shaped tricatenar azobenzenes – Functional liquid crystals with synclinic-anticlinic transitions and spontaneous helix formation

Mohamed Alaasar,[a,b] Silvio Poppe[b] , Yu Cao,[c,d] Changlong, Chen[c], Feng Liu[c] Chenhui Zhu,[d] and Carsten Tschierske[a]

[a] Institute of Chemistry, Martin Luther University Halle-Wittenberg, Kurt Mothes Str. 2, D-06120 Halle (Saale), Germany; carsten.tschierske@chemie.uni-halle.de

[b] Department of Chemistry, Faculty of Science, Cairo University, P.O. 12613 Giza, Egypt; malaasar@sci.cu.edu.eg

[c] State Key Laboratory for Mechanical Behaviour of Materials, School of Materials Science & Engineering, Xi'an Jiaotong University, Xi'an 710049, China; feng.liu@xjtu.edu.cn

[d] Advanced Light Source, Lawrence Berkeley National Laboratory, Berkeley, CA 94720, USA; chenhuizhu@lbl.gov

Contents

1. Methods

Thin layer chromatography (TLC) was performed on aluminium sheet precoated with silica gel. Analytical quality chemicals were obtained from commercial sources and used as obtained. The solvents were dried using the standard methods when required. The purity and the chemical structures of all synthesised materials were confirmed by the spectral data. The structure characterization of the prepared materials is based on ^{1}H-NMR and ^{13}C-NMR (Varian Unity 500 and Varian Unity 400 spectrometers, in $CDCl_3$ solutions, with tetramethylsilane as internal standard). Microanalyses were performed using a Leco CHNS-932 elemental analyzer.

The mesophase behaviour and transition temperatures of the LC materials were measured using a Mettler FP-82 HT hot stage and control unit in conjunction with a Nikon Optiphot-2 polarizing microscope. The associated enthalpies were obtained from DSC-thermograms which were recorded on a Perkin-Elmer DSC-7, heating and cooling rate: 10 K min^{-1}.

The X-ray diffraction patterns were recorded with a 2D detector (Vantec 500, Bruker). Ni filtered and pin hole collimated CuK_{α} radiation was used. The samples were prepared in the isotropic state on a glass slide. The exposure times were 30 min for SAXS and 15 min for WAXS. The sample to detector distance differs from 9.0 cm for WAXS to 26.90 cm for SAXS. Uniform orientation was achieved by slow cooling (0.5 K·min^{-1}) from isotropic state in the LC state. The samples were held on a temperature-controlled heating stage. As a result a XRD pattern was obtained which is transformed to a 1D plot using GADDS over the full Chi range.

High-resolution small-angle powder diffraction experiments were recorded on beamline BL16B1 at Shanghai Synchrotron Radiation Facility, SSRF. Samples were held in evacuated 1 mm capillaries. A modified Linkam hot stage with a thermal stability within 0.2 ºC was used, with a hole for the capillary drilled through the silver heating block and mica windows attached to it on each side. A MarCCD detector was used. *q* calibration and linearization were verified using several orders of layer reflections from silver behemate and a series of *n*-alkanes. The measurement of the positions and intensities of the diffraction peaks is carried out using Galactic PeakSolve^{TM} program, where experimental diffractograms are fitted using Gaussian shaped peaks. The diffraction peaks are indexed on the basis of their peak positions, and the lattice parameters and the space groups are subsequently determined.

Once the diffraction intensities are measured and the corresponding space group determined, 3-d electron density maps can be reconstructed, on the basis of the general formula

$$E(xyz) = \Sigma_{hkl}\, F(hkl)\, \exp[\mathrm{i}2\pi(hx+ky+lz)] \qquad \text{(Eqn. 1)}$$

Here $F(hkl)$ is the structure factor of a diffraction peak with index (hkl). It is normally a complex number and the experimentally observed diffraction intensity

$$I(hkl) = \mathrm{K}\cdot F(hkl)\cdot F^*(hkl) = \mathrm{K}\cdot |F(hkl)|^2 \qquad \text{(Eqn. 2)}$$

Here K is a constant related to the sample volume, incident beam intensity etc. In this paper we are only interested in the relative electron densities, hence this constant is simply taken to be 1. Thus the electron density

$$E(xyz) = \Sigma_{hkl}\, \mathrm{sqrt}[I(hkl)]\, \exp[\mathrm{i}2\pi(hx+ky+lz)+\phi_{hkl}] \qquad \text{(Eqn. 3)}$$

for 2D structures $I(hk)$ and Eqn. (4) were used:

$$E(xy) = \Sigma_{hk}\, \mathrm{sqrt}[I(hk)]\, \exp[i2\pi(hx+ky) +\phi_{hk}] \qquad \text{(Eqn. 4)}$$

As the observed diffraction intensity $I(hkl)$ is only related to the amplitude of the structure factor $|F(hkl)|$, the information about the phase of $F(hkl)$, ϕ_{hkl}, can not be determined directly from experiment. However, the problem is much simplified when the structure of the ordered phase is centrosymmetric, and hence the structure factor $F(hkl)$ is always real and ϕ_{hkl} is either 0 or π.

This makes it possible for a trial-and-error approach, where candidate electron density maps are reconstructed for all possible phase combinations, and the "correct" phase combination is then selected on the merit of the maps, helped by prior physical and chemical knowledge of the system. This is especially useful for the study of nanostructures, where normally only a limited number of diffraction peaks are observed.

Resonant Soft X-ray Scattering (RSoXS) was recorded on BL11.1.0.2, Advanced Light Source, ALS. Sample film was prepared by drop-casting between two pieces of silicon nitride glass. The glass thickness is 100nm and sample film is ~500nm to confirm the penetration of soft X-ray around 284eV. To reduce attenuation, it was essential to keep both sample and CCD detector in a vacuum chamber, at $p = 10^{-6}$ Torr. A self made hot stage was

used. Temperature difference due to high vacuum in chamber has been calibrated. The scattering intensity was recorded by a back illuminated Princeton PI-MTE CCD thermoelectrically cooled to −45 °C. The CCD pixel size is 0.027 mm and the detector is positioned 48.47 mm away from the sample. q calibration was conducted with bent-core material whose commercial name is NOBOW at C K edge. To collect data at high q range, CCD is moved horizontally up to 40mm away from original position. The covered q range is calculated from beam stop edge to far edge of CCD at 40 mm away. The exposure time used is 30-120s. The X-ray beam (300 × 200 μm^2) is linearly polarized. The collected data was subsequently converted to one-dimensional line profiles using the Nika software package, where experimental diffractograms are fitted using Gaussian shaped peaks.

2. Additional data

2.1 DSC traces

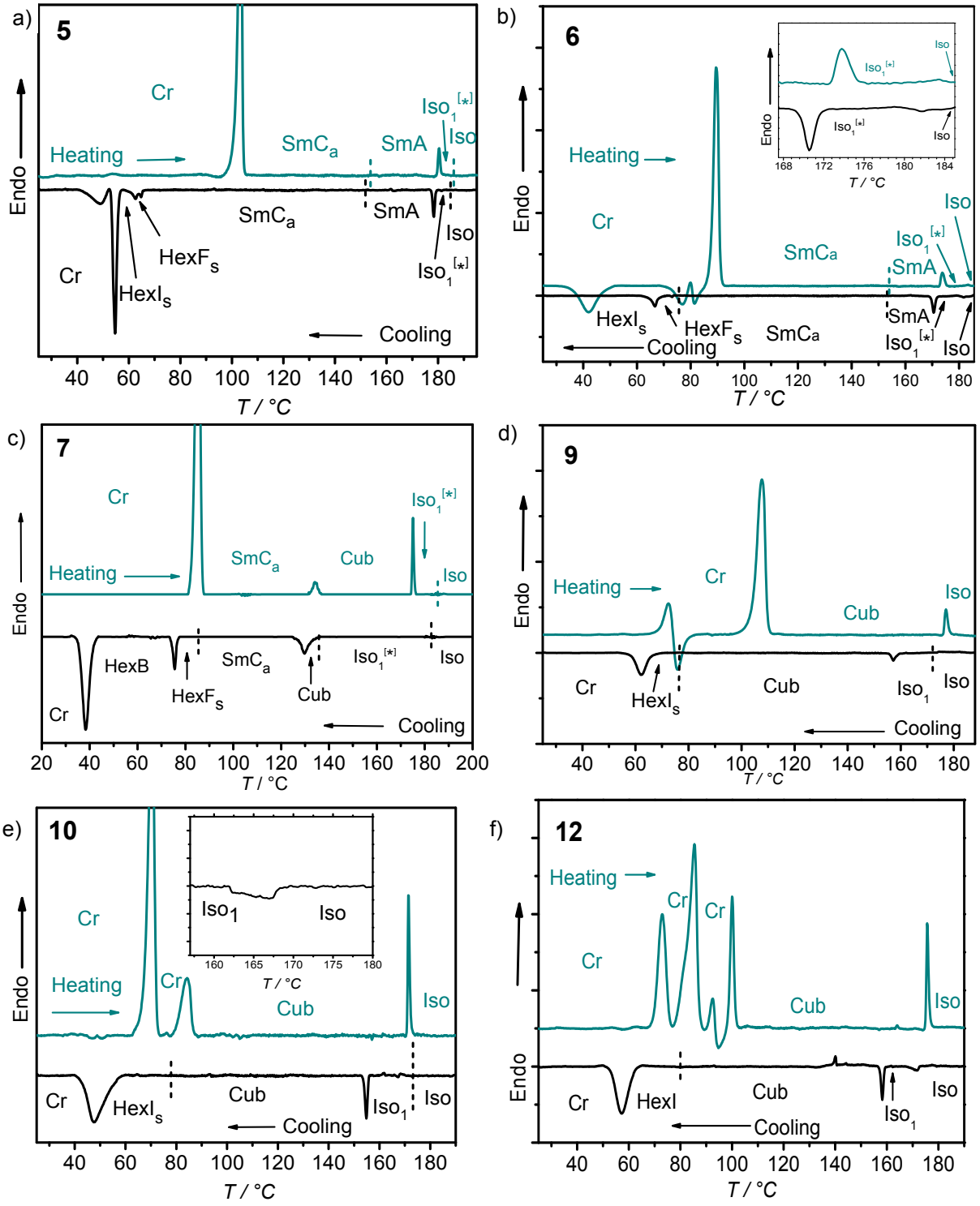

Figure S1. DSC heating and cooling curves (10 K min^{-1}) of compounds **5-7** and **9-12**, for DSC of compound **4**, see ref.[S1,S2]; Cub = Cub$_{bi}$/*Ia*$\bar{3}$*d*; the absence of an enthalpy for the Cub-HexI transition is due to the slow transition.

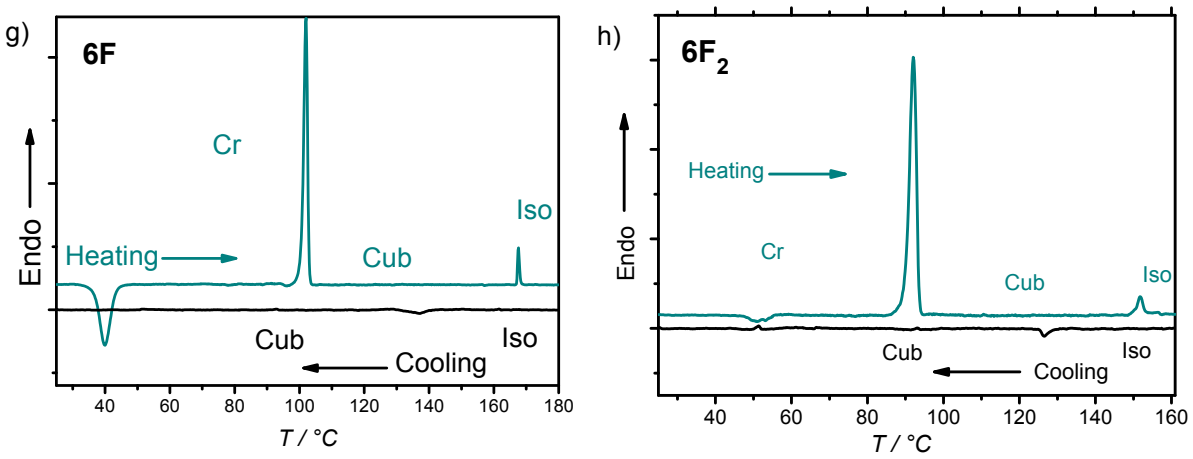

Figure S1 (continued). DSC heating and cooling traces (10 K min^{-1}) of compounds **6F** and **$6F_2$**.

2.2. Textures

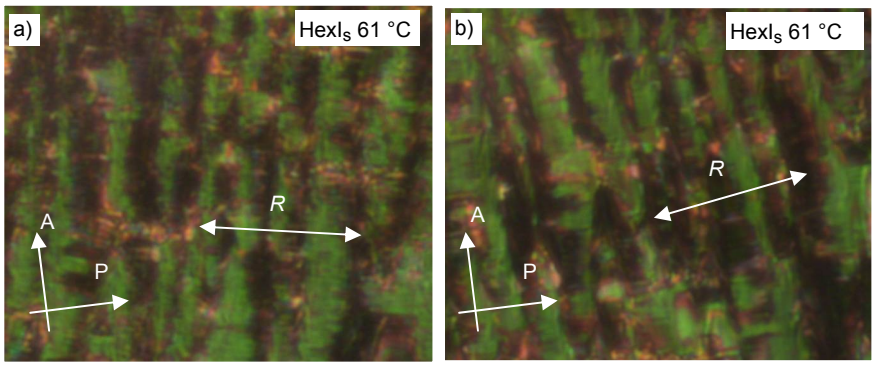

Figure S2. Texture of the $HexI_s$ phase of compound **5** after slight rotation of the sample, indicating a tilt of 8-10° (6 µm ITO cell, R = rubbing direction).

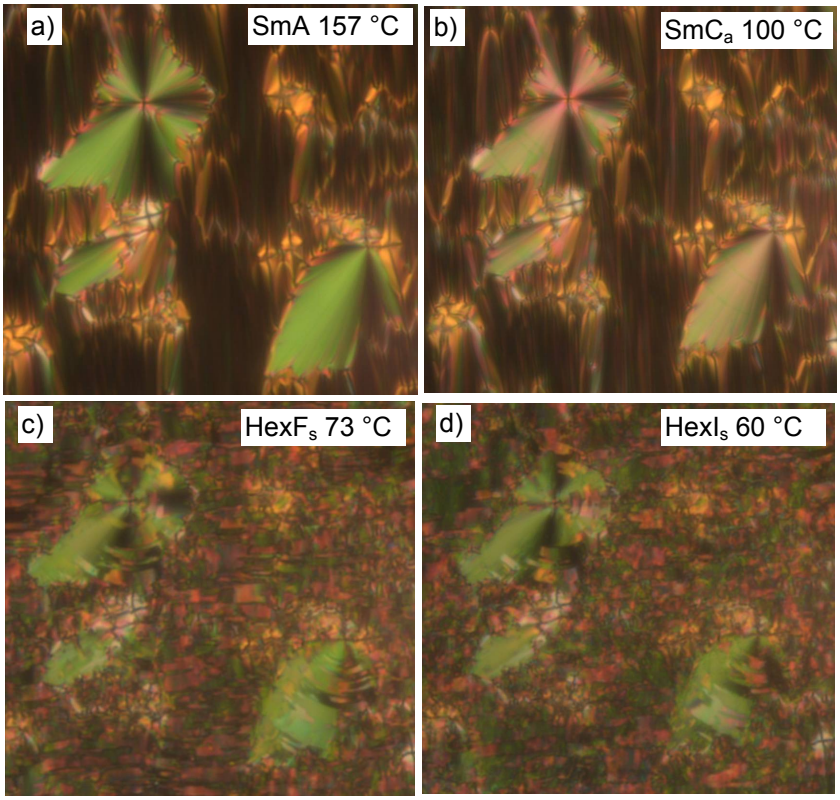

Figure S3. Textures of compound **6** as observed on cooling in planar cells (6 μm PI-coated ITO cell) in the designated phases at the given temperatures.

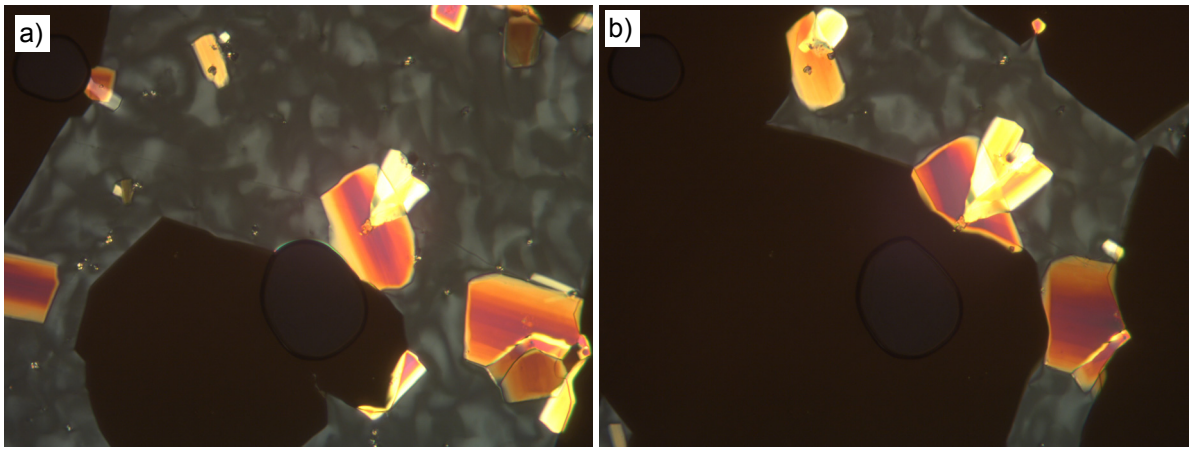

Figure S4. Transition from the SmC$_a$ phase to the Cub$_{bi}$/*Ia*$\bar{3}$*d* phase with a birefringent M phase occurring as metastable intermediate phase coexisting with Cub and SmC$_a$, as observed on heating compound **7**, a) at T = 134 °C and b) at 135 °C.

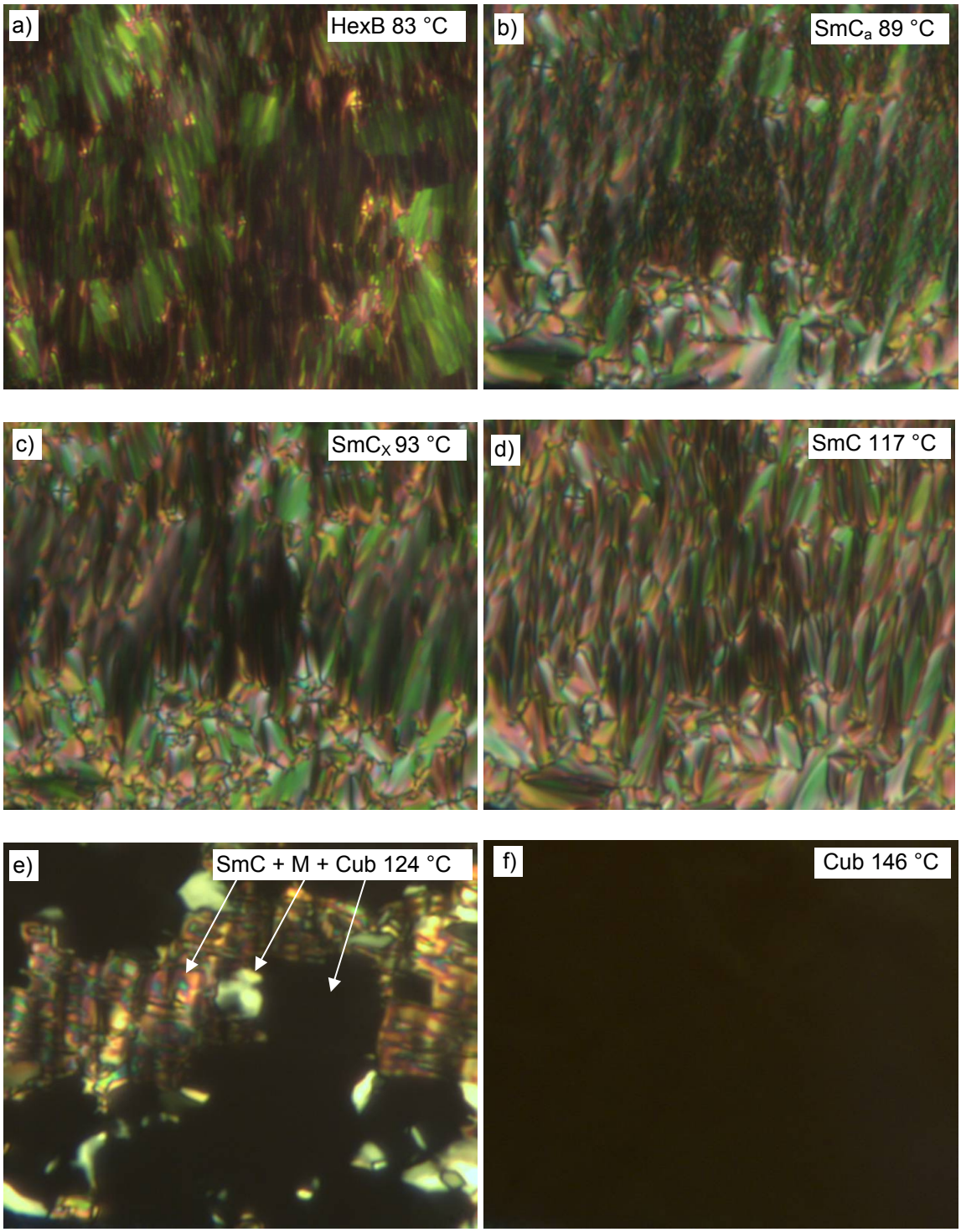

Figure S5. Textures of compound **8** as observed on heating in planar alignment (in a 6 μm PI-coated ITO cell) at the given temperatures in the indicated phases.

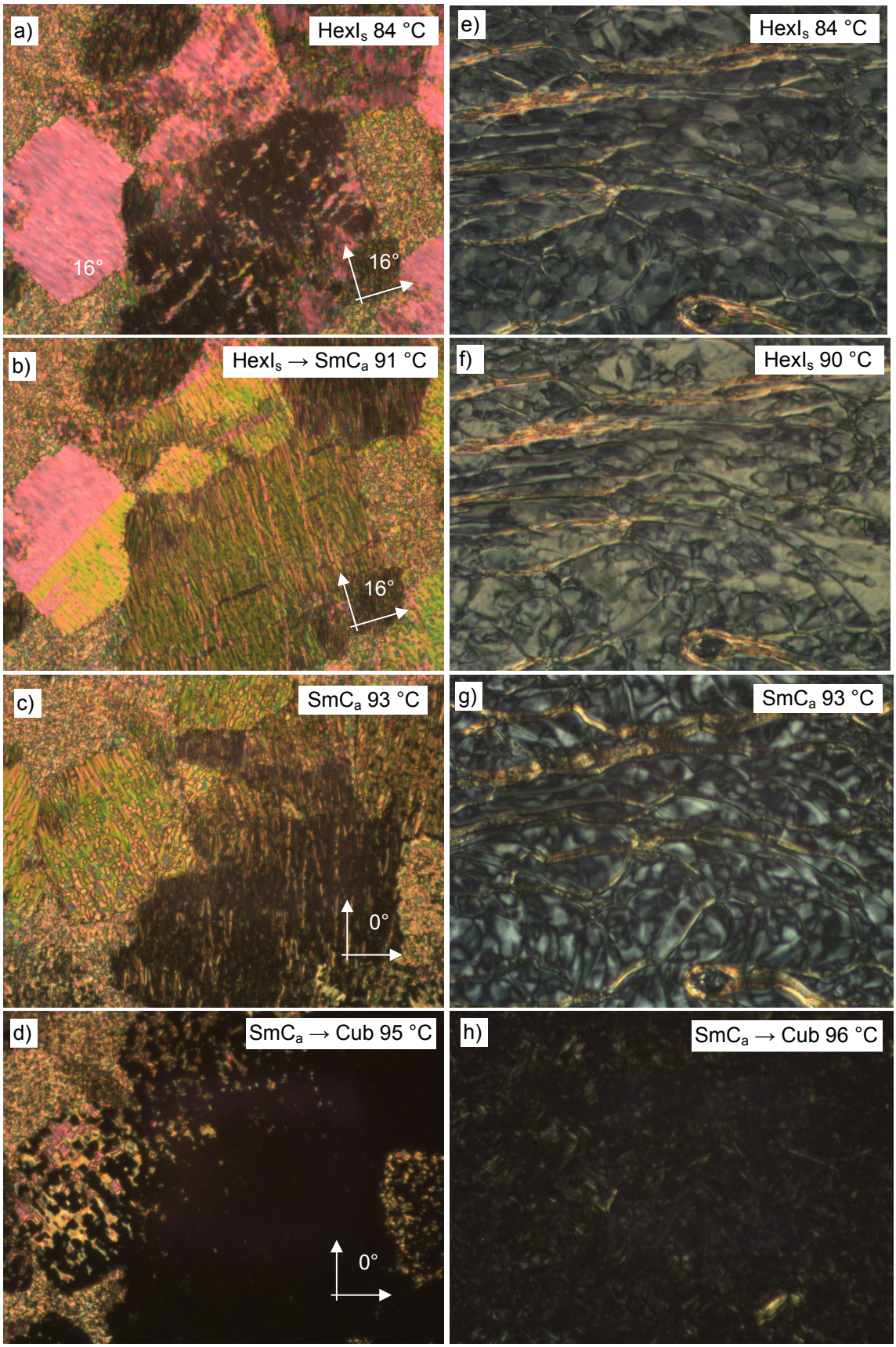

Figure S6. Textures of compound **9** as observed on heating in planar alignment (left, 6 µm PI-coated ITO cell) and homeotropic alignment (right, between plain microscopy glass plates) at the given temperatures in the indicated phases.

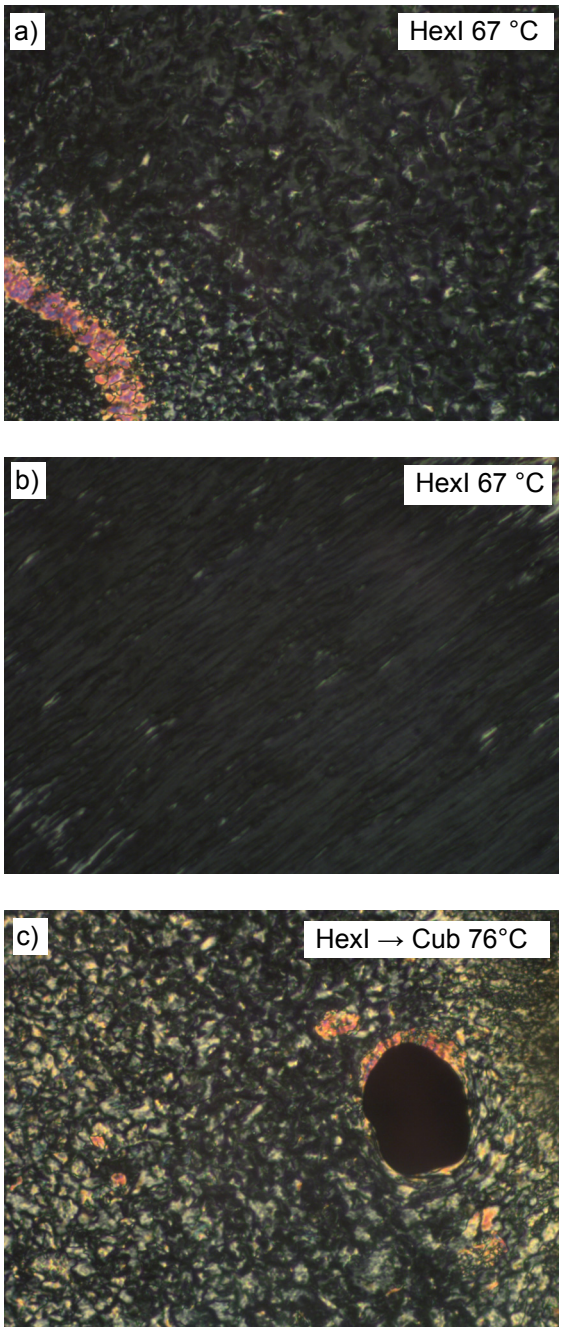

Figure S7. a, c) Weakly birefringent homeotropic textures of compound **12** as observed on heating between plain microscopy glass plates at the given temperatures (high birefringence areas represent planar aligned regions); a) HexI phase, b) texture after shearing retains the weak birefringence and hence suggest a biaxial hexatic phase in the whole mesomorphic temperature range below the cubic phase, c) shows the development of the cubic phase (starting in samples between glass plates already at 76 °C and thus deviating from the DSC data).

2.3 XRD Data

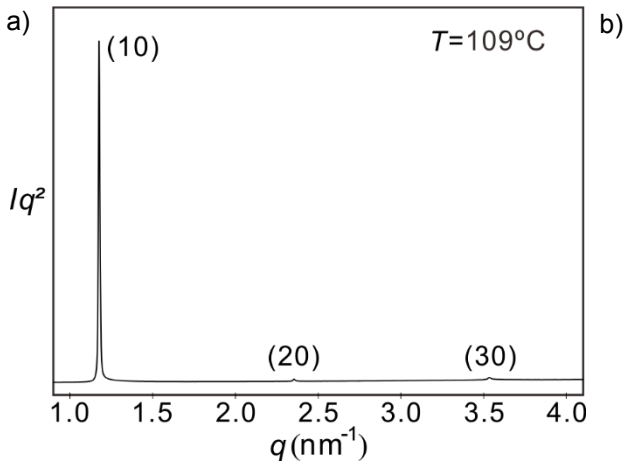

Figure S8. a) SAXS diffractogram of compound **7** at 109 ºC.

Table S1. Experimental and calculated *d*-spacing of the observed SAXS reflection of the lamellar phase in **7** at 109 ºC. All intensity values are Lorentz and multiplicity corrected.

(*hk*)	$d_{obs.}$ – spacing (nm)	$d_{cal.}$ – spacing (nm)	*intensity*	*Phase*
(10)	5.34	5.34	100.0	π
(20)	2.67	2.67	0.9	π
(30)	1.78	1.78	1.8	π
d = 5.34 nm				

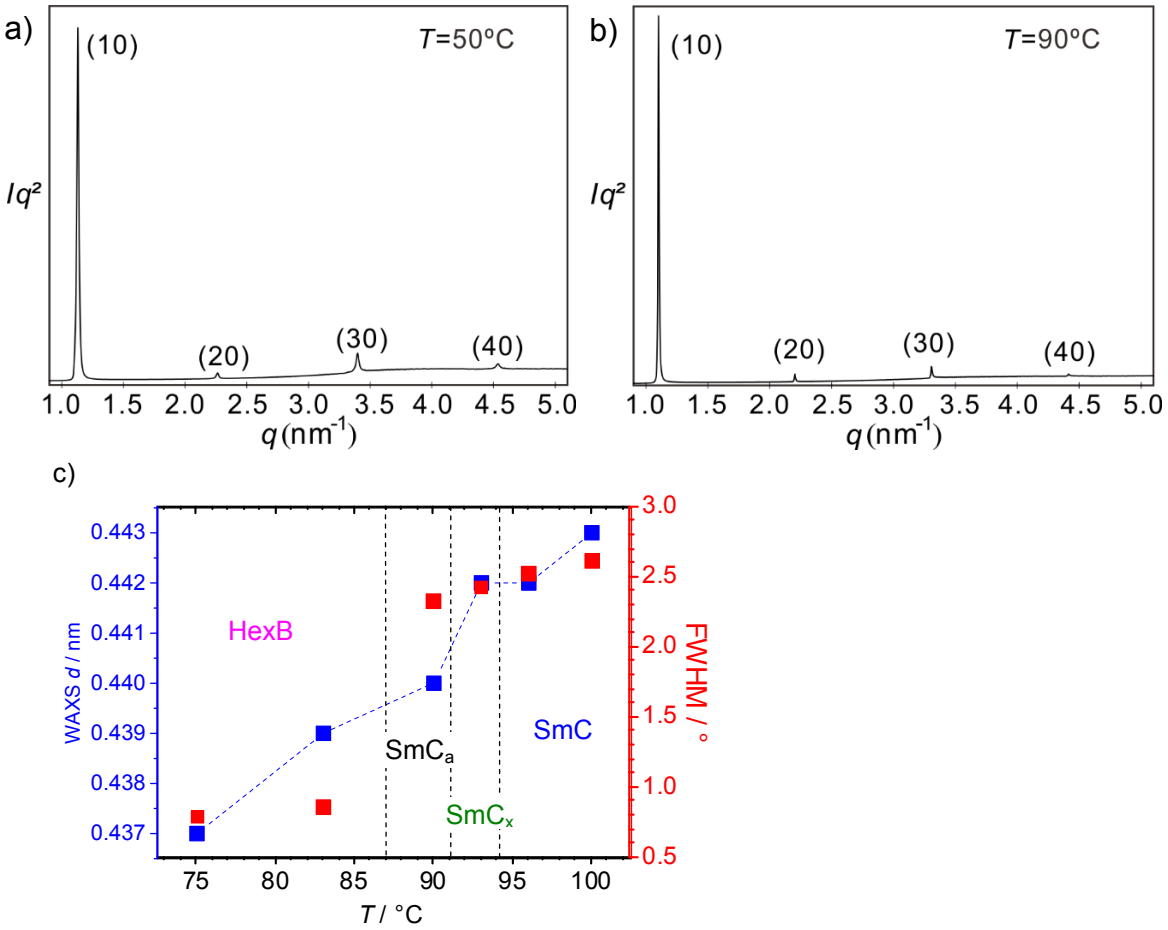

Figure S9. a, b) SAXS diffractograms of compound **8** a) in the HexB phase at 50 °C (d = 5.70 nm) and b) in the SmC_a phase at 90 °C (d = 5.56 nm) and c) WAXS data showing the position of the maximum and FWHM.

Table S2. Experimental and calculated d-spacing of the observed SAXS reflection of the lamellar phase (HexB) in **8** at cooling at 50 ºC. All intensity values are Lorentz and multiplicity corrected.

(*hk*)	$d_{obs.}$ – spacing (nm)	$d_{cal.}$ – spacing (nm)	*intensity*	*Phase*
(10)	5.56	5.56	100.0	π
(20)	2.78	2.78	2.0	π
(30)	1.85	1.85	8.6	π
(40)	1.39	1.39	3.0	π
d = 5.56 nm				

Table S3. Experimental and calculated *d*-spacing of the observed SAXS reflection of the lamellar phase (SmC_a) in **8** at cooling at 90 ºC. All intensity values are Lorentz and multiplicity corrected.

(*hk*)	$d_{obs.}$ – spacing (nm)	$d_{cal.}$ – spacing (nm)	*intensity*	*Phase*
(10)	5.70	5.70	100.0	π
(20)	2.85	2.85	2.4	π
(30)	1.90	1.90	4.3	π
(40)	1.42	1.42	0.9	π
d = 5.70 nm				

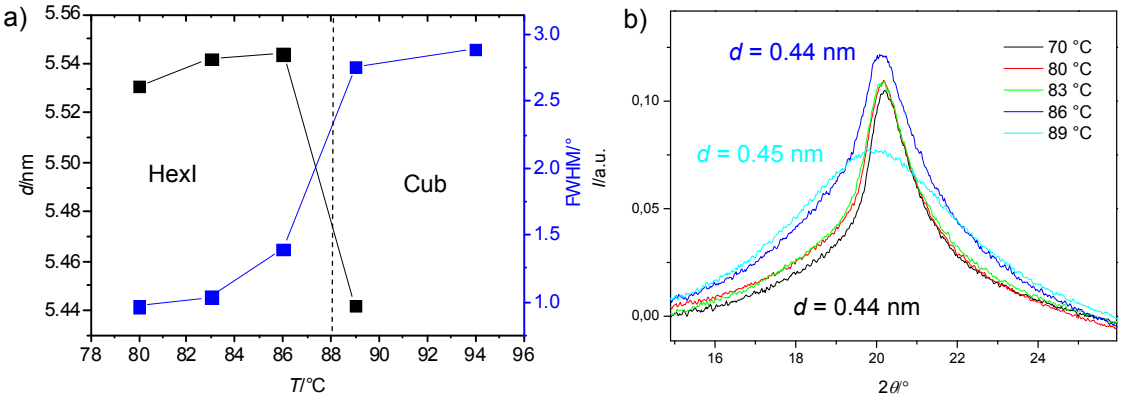

Figure S10: XRD of compound **9** in the different mesophases: a) temperature dependence of *d*-spacings and line width of the layer reflections in the SAXS patterns and b) WAXS as a function of temperature.

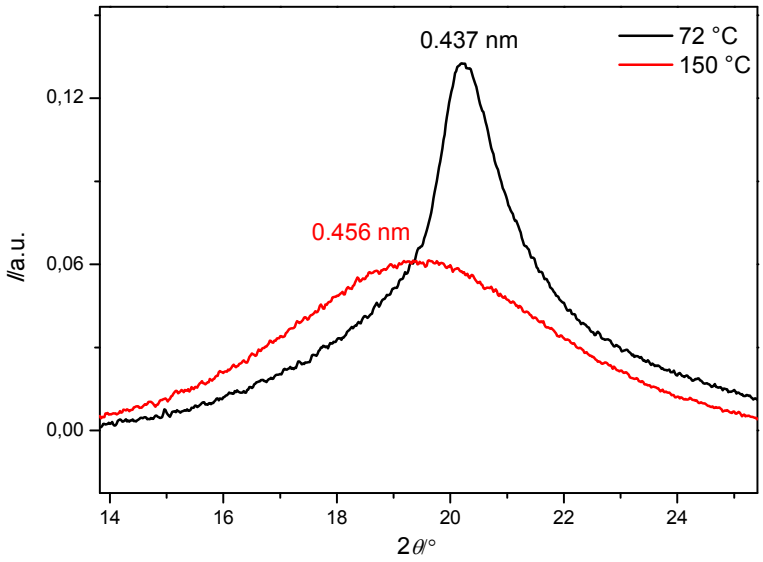

Figure S11. Maxima of the WAXS of compound **12** in the HexB (T = 72 °C) and the $Cub_{bi}/Ia\bar{3}d$ phase (T = 150 °C).

Table S4. Experimental and calculated *d*-spacing of the observed SAXS reflection of the $Cub_{bi}/Ia\bar{3}d$ phase in **6F** at 135 ºC. All intensity values are Lorentz and multiplicity corrected.

(*hkl*)	$d_{obs.}$ – spacing (nm)	$d_{cal.}$ – spacing (nm)	*intensity*	*Phase*
(211)	3.87	3.87	100.0	π
(220)	3.35	3.35	54.3	π
(321)	2.53	2.53	0.04	π
(400)	2.37	2.37	3.3	π
(420)	2.12	2.12	0.8	π
(332)	2.02	2.02	0.8	0
(422)	1.93	1.93	0.2	π
(431)	1.86	1.86	0.09	π
a_{cub} = 9.48 nm				

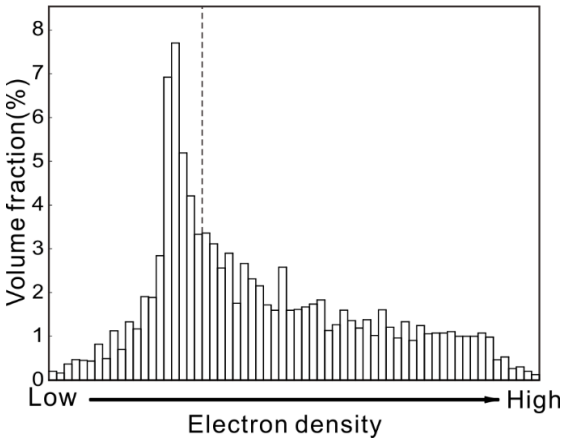

Figure S12. Histogram of the electron density map of compound **6F**.

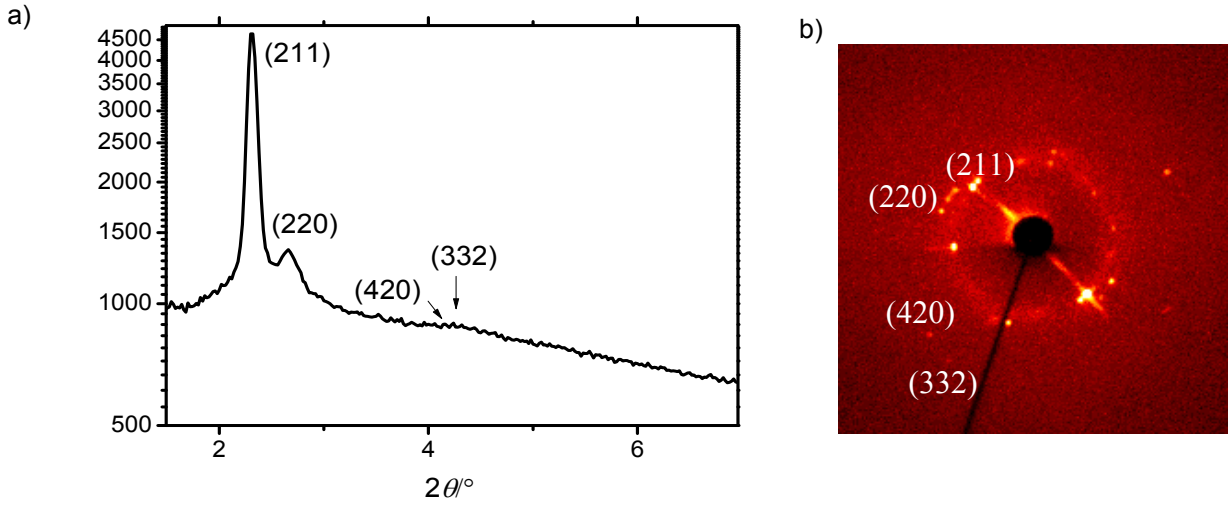

Figure S13. SAXS patterns in the $Cub_{bi}/Ia\bar{3}d$ phase of compound $\mathbf{6F_2}$ at 120 °C and indexation.

Table S5. XRD data of the $Cub_{bi}/Ia\bar{3}d$ phases of compounds **9-12** and **6F$_2$**.

Compd.	(*hkl*)	d_{obs} – spacing (nm)	d_{calc} – spacing (nm)	d_{obs} - d_{calc}	a_{cub}/nm (T/°C)
9	(211)	4.249	4.249	0.00	10.41 (94 °C)
	(220)	3.686	3.686	0.00	
10	(211)	3.918	3.918	0.00	9.60 (150 °C)
	(220)	3.408	3.393	0.02	
	(420)	2.146	2.146	0.00	
12	(211)	4.134	4.134	0.00	10.13 (150 °C)
	(220)	3.595	3.580	0.02	
6F$_2$	(211)	3.818	3.818	0.00	9.35 (120 °C)
	(220)	3.331	3.306	0.03	
	(420)	2.143	2.091	0.05	
	(332)	2.040	1.994	0.05	

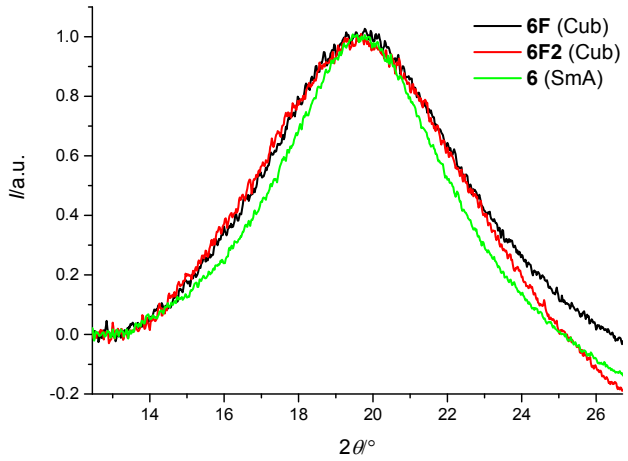

Figure S14. Maxima of the WAXS of the nonfluorinated compound **6** and the fluorinated compounds **6F** and **6F$_2$** at T = 120 °C in the indicated phases.

2.4 RSoXS data

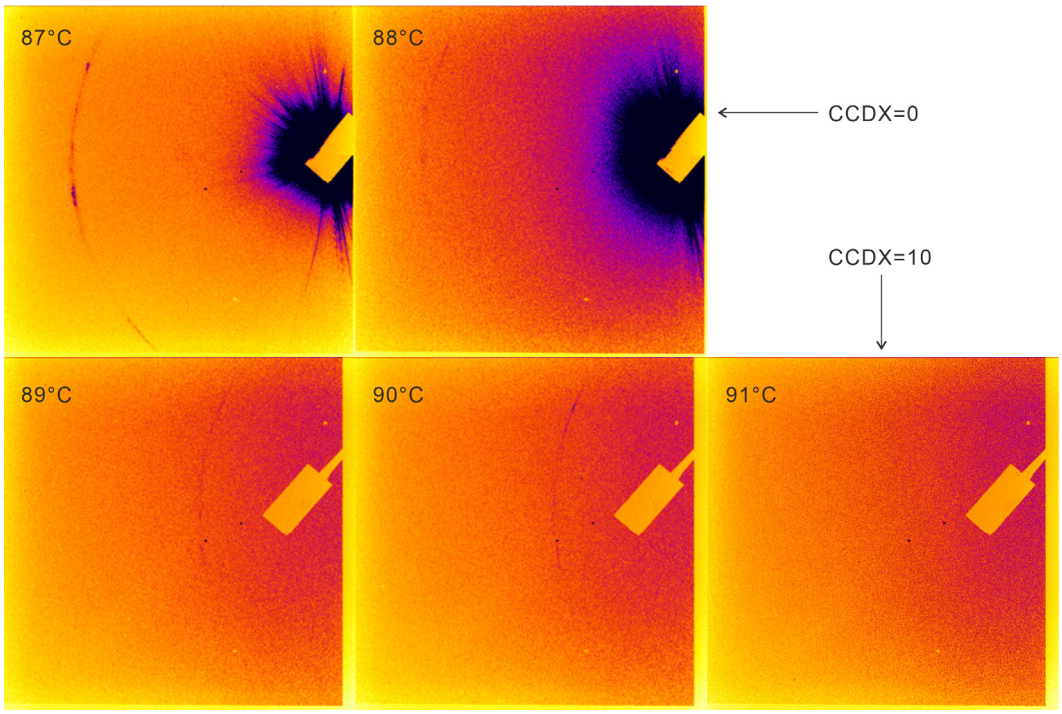

Figure S15. CCD images of pure resonant peak upon heating. The resonant signal is too weak for temperature higher than 89 °C. CCD was moved 10 mm left avoiding central beam to conduct longer exposure. When temperature reached 91 °C, resonant signal disappeared.

Table S6. Position of the resonant peak at different temperatures.

T /°C	d_{res}/nm	d_{res}/d_0
87	11.24	1.99
88	11.03	1.96
89	11.08	1.97
90	11.16	1.98

3. Synthesis and Analytical Data

The synthesis of the new polycatenars is shown in **Scheme S1**. Compounds **4-12** without fluorine substitution was prepared starting from the benzoic acid derivatives (**1/n**),[S2] while those with one or two fluorine substitution was done using the fluorinated benzoic acid derivatives **1/6F** or **1/6F$_2$** which were prepared using similar procedure to that reported recently by us.[S4]

General Procedure. The target compounds were synthesized in analogous way to that used for compounds **4-8**[S1] as follow:
1.0 mmol of the acid **1/n**, **1/6F** or **1/6F$_2$** was converted to the corresponding acid chloride by refluxing with excess thionyl chloride and two drops of *N,N*-dimethylformamide for one hour. After removing the excess of thionyl chloride by distillation under reduced pressure, 4,4'-dihydroxybiphenyl [S1] (1.0 mmol) dissolved in dry dichloromethane was added followed by

addition of triethylamine (1.2 mmol) and a catalytic amount of pyridine. The reaction mixture was then refluxed for 6 hours under an argon atmosphere. After reaction completeness the solution extracted with dichloromethane and washed with 10% HCl and water and finally dried over anhydrous sodium sulphate. An orange solid material was obtained after removing the solvent, which was then chromatographed on silica gel using dichloromethane followed by recrystallization from chloroform/ethanol mixture (1/1) to give the final materials. The analytical data obtained for the new materials **9-12**, **6F** and **$6F_2$** are given below.

3.1 Compounds 9-12

Compound 9. Orange crystals, yield = 72.3 %; ^{1}H NMR (400 MHz, $CDCl_3$) δ 8.36 (d, *J* = 8.7 Hz, 2H, Ar-H), 8.04 – 7.93 (m, 4H, Ar-H), 7.73 – 7.60 (m, 4H, Ar-H), 7.40 – 7.27 (m, 6H, Ar-H), 7.03 (d, *J* = 8.7 Hz, 2H, Ar-H), 6.73 (t, *J* = 2.3 Hz, 1H, Ar-H), 4.12 – 3.97 (m, 6H, -O$\underline{CH_2}CH_2$), 1.91 – 1.73 (m, 6H, -$OCH_2\underline{CH_2}$), 1.60 – 1.20 (m, 24H, CH_2), 1.00 – 0.83 (m, 9H, CH_3). ^{13}C NMR (101 MHz, $CDCl_3$) δ 165.08, 164.74, 162.47, 160.31, 155.86, 150.49, 150.42, 146.87, 138.29, 138.15, 131.22, 131.11, 130.35, 128.23, 128.20, 125.29, 122.51, 122.03, 114.83, 108.23, 107.19, 68.47, 68.43, 31.86, 31.54, 29.51, 29.36, 29.23, 29.14, 25.99, 25.68, 22.65, 22.58, 14.09, 14.01. Elemental analysis, calc. For $C_{53}H_{64}N_2O_7$: C 75.68%, H 7.67%, N 3.33% , found: C 75.64%, H 7.65%, N 3.31%.

Compound 10. Orange crystals, yield = 71.9 %; ^{1}H NMR (500 MHz, $CDCl_3$) δ 8.36 (d, *J* = 8.8 Hz, 2H, Ar-H), 8.03 – 7.93 (m, 4H, Ar-H), 7.70 – 7.62 (m, 4H, Ar-H), 7.39 – 7.27 (m, 6H, Ar-H), 7.03 (d, *J* = 8.7 Hz, 2H, Ar-H), 6.73 (t, *J* = 2.3 Hz, 1H, Ar-H), 4.11 – 3.98 (m, 6H, -O$\underline{CH_2}CH_2$), 1.91 – 1.71 (m, 6H, -$OCH_2\underline{CH_2}$), 1.60 – 1.18 (m, 26H, CH_2), 0.99 – 0.83 (m, 9H, CH_3). ^{13}C NMR (126 MHz, cdcl$_3$) δ 165.07, 164.74, 162.48, 160.31, 155.86, 150.50, 150.42, 146.87, 138.29, 138.15, 131.22, 131.11, 130.35, 128.23, 128.19, 125.29, 122.51, 122.03, 122.02, 121.94, 114.83, 108.23, 107.19, 68.46, 68.43, 31.88, 31.54, 29.55, 29.53, 29.36, 29.29, 29.14, 25.99, 25.68, 22.60, 22.66, 22.58, 14.01, 14.00. Elemental analysis, calc. For $C_{54}H_{66}N_2O_7$: C 75.85%, H 7.78%, N 3.28% , found: C 75.79%, H 7.74%, N 3.28%.

Compound 12. Orange crystals, yield = 72.5 %; ^{1}H NMR (400 MHz, $CDCl_3$) δ 8.36 (d, *J* = 8.8 Hz, 2H, Ar-H), 8.03 – 7.93 (m, 4H, Ar-H), 7.72 – 7.60 (m, 4H, Ar-H), 7.38 – 7.27 (m, 6H, Ar-H), 7.03 (d, *J* = 8.8 Hz, 2H, Ar-H), 6.73 (t, *J* = 2.3 Hz, 1H, Ar-H), 4.12 – 3.95 (m, 6H, -O$\underline{CH_2}CH_2$), 1.90 – 1.69 (m, 6H, -$OCH_2\underline{CH_2}$), 1.61 – 1.20 (m, 30H, CH_2), 1.01 – 0.83 (m, 9H, CH_3). ^{13}C NMR (126 MHz, $CDCl_3$) δ 165.07, 164.74, 162.48, 160.31, 155.86, 150.50, 150.42, 146.87, 138.28, 138.15, 131.22, 131.11, 130.35, 128.23, 128.19, 125.29, 122.52, 122.03, 122.02, 114.83, 108.23, 107.19, 68.47, 68.43, 31.88, 31.54, 29.55, 29.53, 29.36, 29.29, 29.15, 29.14, 25.99, 25.68, 22.66, 22.58, 14.09, 14.00. Elemental analysis, calc. For $C_{56}H_{70}N_2O_7$: C 76.16%, H 7.99%, N 3.17% , found: C 76.14%, H 7.99%, N 3.17%.

3.2 Compounds 6F and $6F_2$

Compound 6F. Orange crystals, yield = 73.0 %; ^{1}H NMR (400 MHz, $CDCl_3$) δ 8.36 (d, *J* = 8.4 Hz, 2H, Ar-H), 7.99 (d, *J* = 8.3 Hz, 2H, Ar-H), 7.83 (dd, *J* = 8.6, 2.3 Hz, 1H, Ar-H), 7.75 (dd, *J* = 11.9, 2.3 Hz, 1H, Ar-H), 7.70 – 7.60 (m, 4H, Ar-H), 7.39 – 7.27 (m, 6H, Ar-H), 7.10 (t, *J* = 8.6 Hz, 1H, Ar-H), 6.73 (t, *J* = 2.3 Hz, 1H, Ar-H), 4.14 (t, *J* = 6.6 Hz, 2H, -O$\underline{CH_2}CH_2$), 4.02 (t, *J* = 6.5 Hz, 4H, -O$\underline{CH_2}CH_2$), 1.96 – 1.71 (m, 6H, -$OCH_2\underline{CH_2}$), 1.60 – 1.27 (m, 18H, CH_2), 1.01 – 0.82 (m, 9H, CH_3). ^{13}C NMR (126 MHz, $CDCl_3$) δ 165.07, 164.65, 160.31, 155.46, 150.76, 150.51, 150.39, 146.49, 138.33, 138.13, 131.25, 131.11, 130.79, 128.24, 128.19, 123.79, 122.68, 122.04, 121.99, 113.47, 108.23, 107.93, 107.77, 107.19, 69.55, 68.43, 31.54, 31.50, 29.14, 29.02, 25.68, 25.56, 22.58, 22.55, 14.00, 13.99. ^{19}F NMR (376 MHz,

$CDCl_3$): δ (ppm) = -132.58 – -132.62 (m). Elemental analysis, calc. For $C_{50}H_{57}FN_2O_7$: C 73.51%, H 7.03%, N 3.43% , found: C 73.44%, H 6.96%, N 3.40%.

Compound 6F$_2$. Orange crystals, yield = 72.75 %; ^{1}H NMR (500 MHz, $CDCl_3$) δ 8.37 (d, *J* = 8.5 Hz, 2H, Ar-H), 8.03 (d, *J* = 8.3 Hz, 2H, Ar-H), 7.71 – 7.56 (m, 5H, Ar-H), 7.39 – 7.27 (m, 6H, Ar-H), 6.88 – 6.77 (m, 1H, Ar-H), 6.72 (t, *J* = 2.3 Hz, 1H, Ar-H), 4.15 (t, *J* = 6.6 Hz, 2H, -O$\underline{CH_2}CH_2$), 4.02 (t, *J* = 6.5 Hz, 4H, -O$\underline{CH_2}CH_2$), 1.96 – 1.72 (m, 6H, -OCH$_2\underline{CH_2}$), 1.61 – 1.28 (m, 18H, CH_2), 1.00 – 0.84 (m, 9H, CH_3). ^{13}C NMR (126 MHz, $CDCl_3$) δ 165.07, 164.58, 160.31, 155.61, 150.52, 150.36, 140.63, 138.35, 138.12, 135.58, 135.54, 131.26, 131.16, 131.11, 128.25, 128.20, 122.93, 122.04, 121.98, 111.97, 111.94, 108.46, 108.23, 107.19, 70.07, 68.43, 31.54, 31.46, 29.14, 29.00, 25.68, 25.49, 22.58, 22.53, 14.00, 13.97. ^{19}F NMR (376 MHz, $CDCl_3$): δ (ppm) = -146.08 – -146.14 (m), -158.05 – -158.11 (m). Elemental analysis, calc. For $C_{50}H_{56}F_2N_2O_7$: C 71.92%, H 6.76%, N 3.35% , found: C 71.87%, H 6.70%, N 3.31%.

3.3 Representative NMR spectra

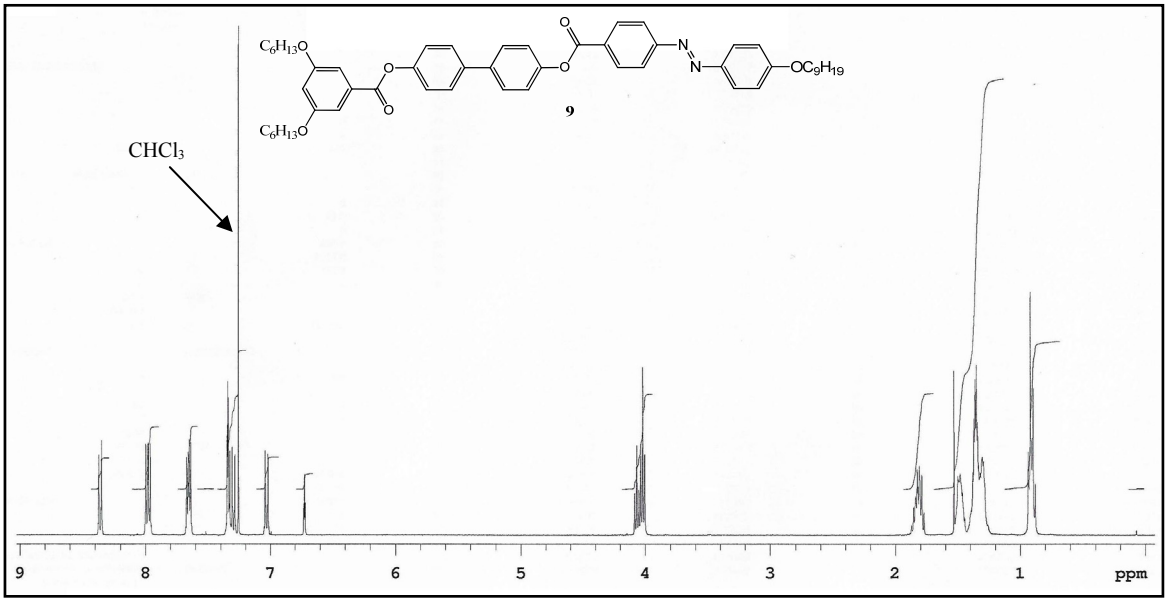

Figure S16. ^{1}H NMR Spectrum of **9** (400 MHz, $CDCl_3$).

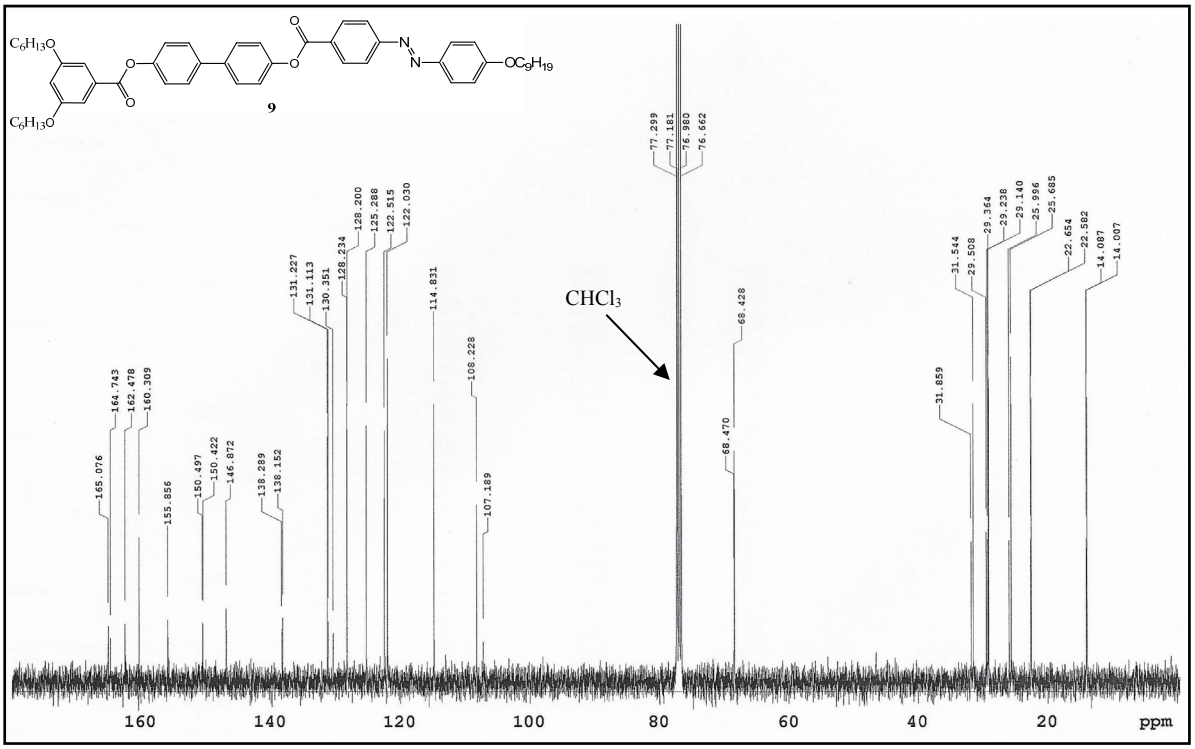

Figure S17. ^{13}C NMR Spectrum of **9** (101 MHz, $CDCl_3$).

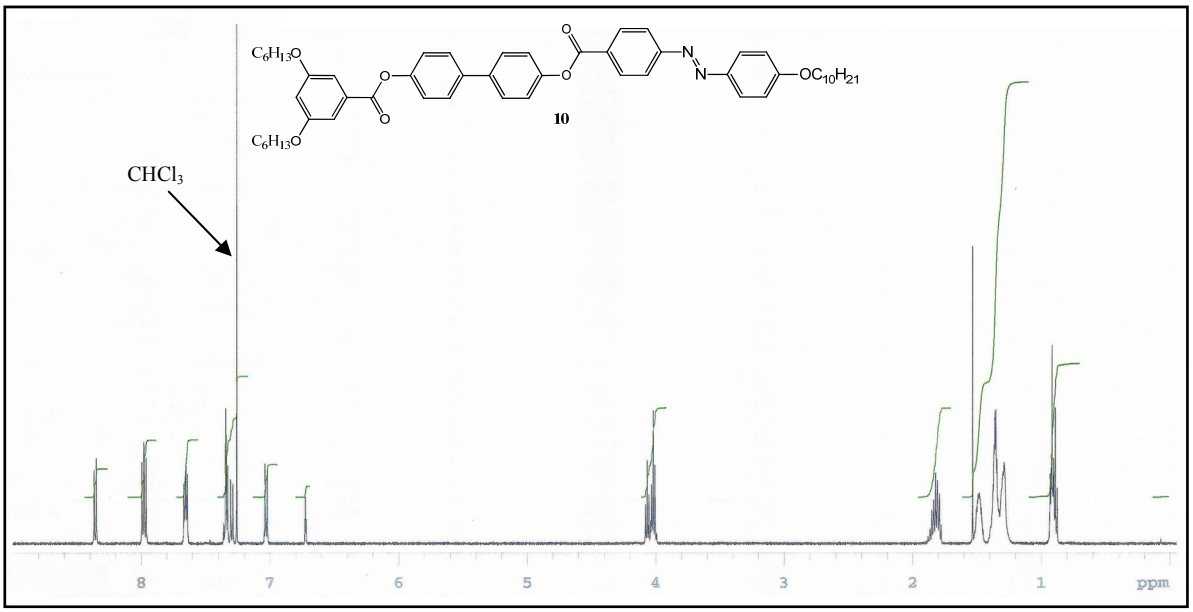

Figure S18. ^{1}H NMR Spectrum of **10** (500 MHz, $CDCl_3$).

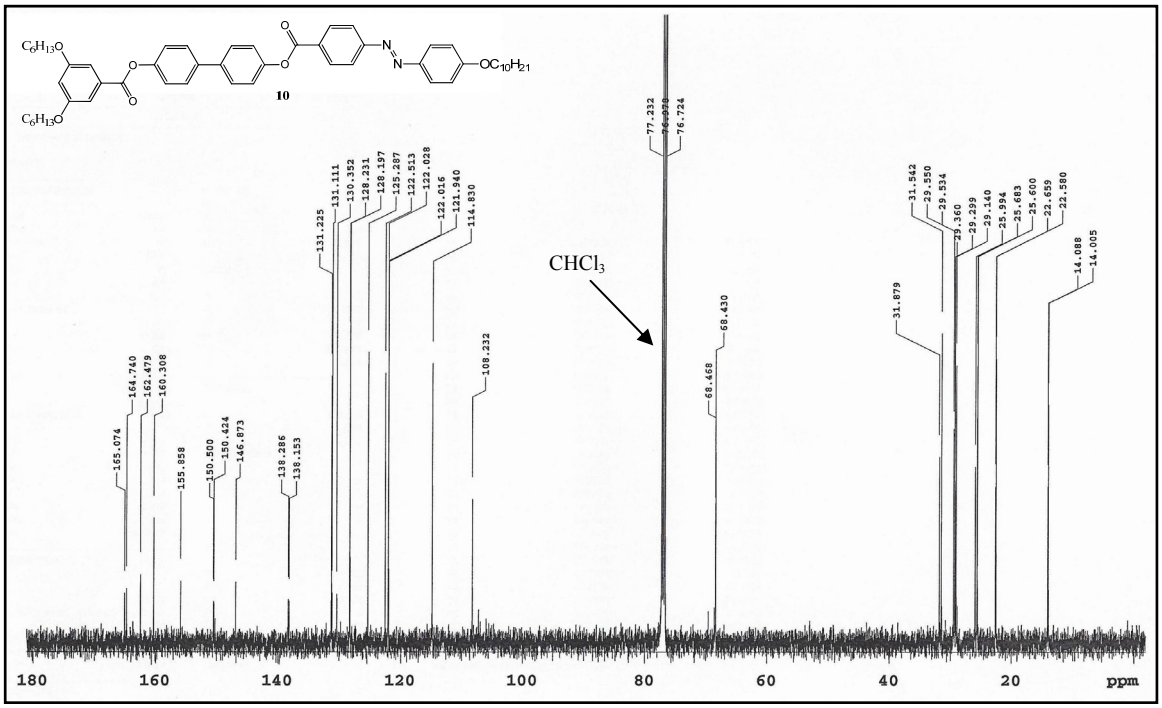

Figure S19. ^{13}C NMR Spectrum of **10** (126 MHz, $CDCl_3$).

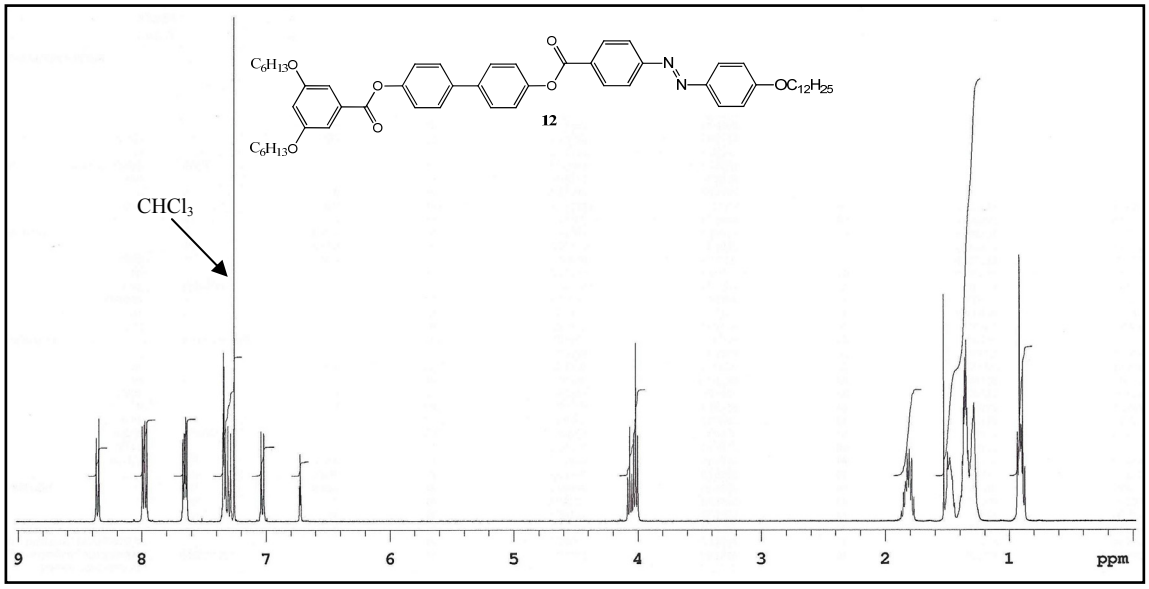

Figure S20. ^{1}H NMR Spectrum of **12** (400 MHz, $CDCl_3$).

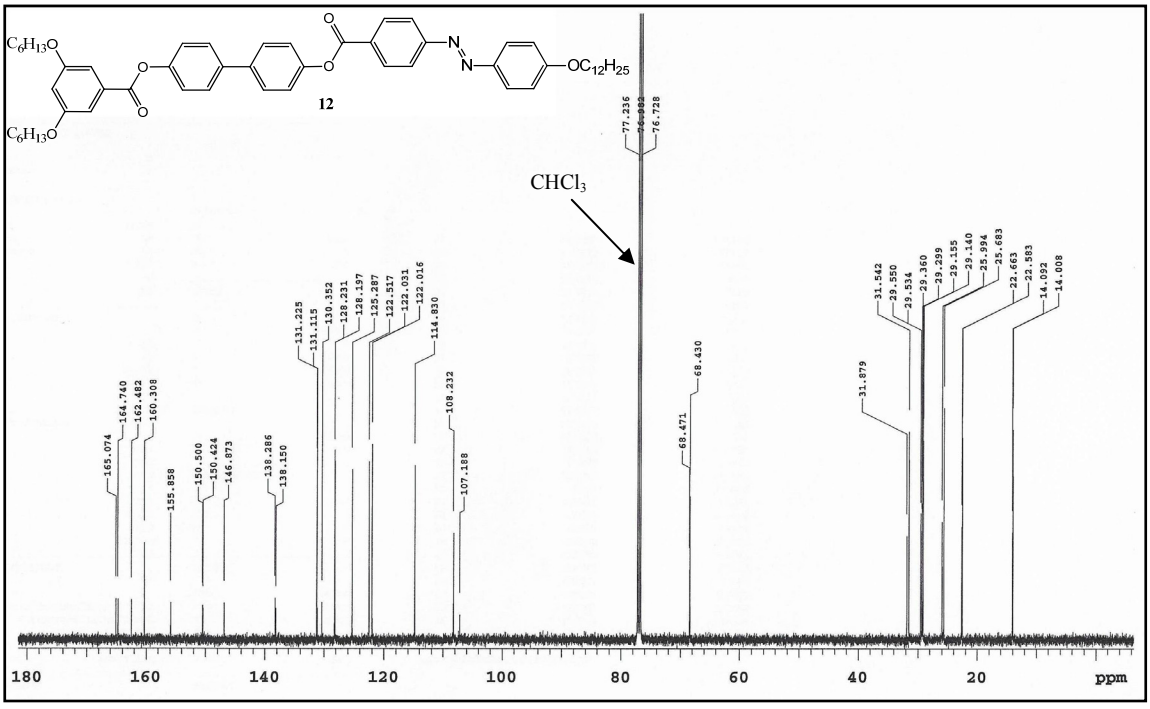

Figure S21. ^{13}C NMR Spectrum of **12** (126 MHz, $CDCl_3$).

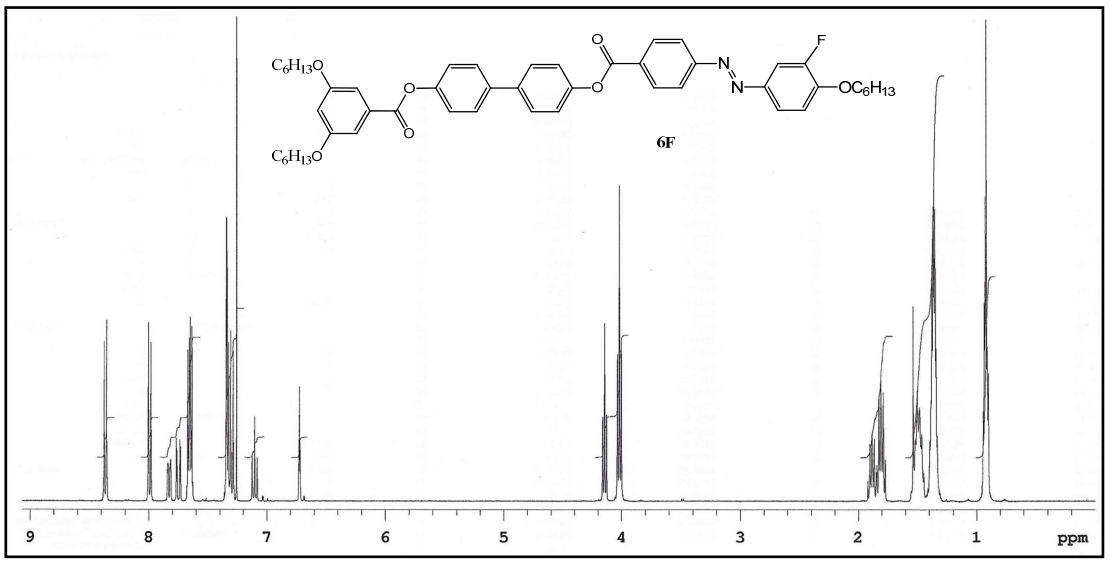

Figure S22. ^{1}H NMR Spectrum of **6F** (400 MHz, $CDCl_3$).

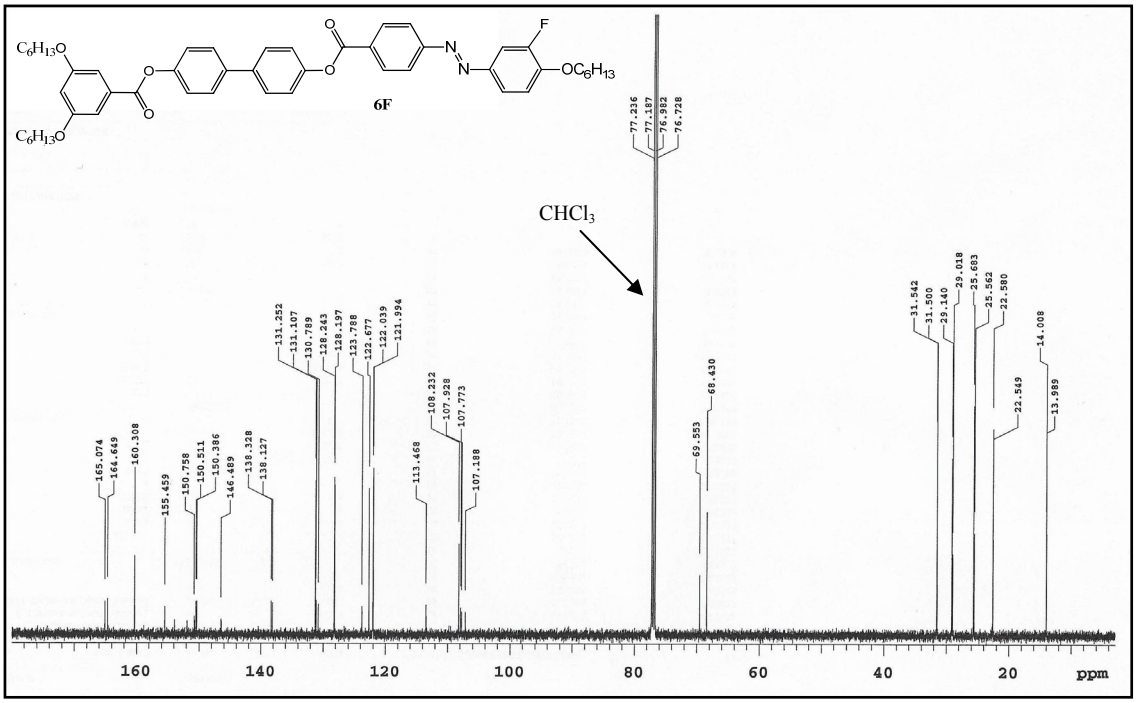

Figure S23. ^{13}C NMR Spectrum of **6F** (126 MHz, $CDCl_3$).

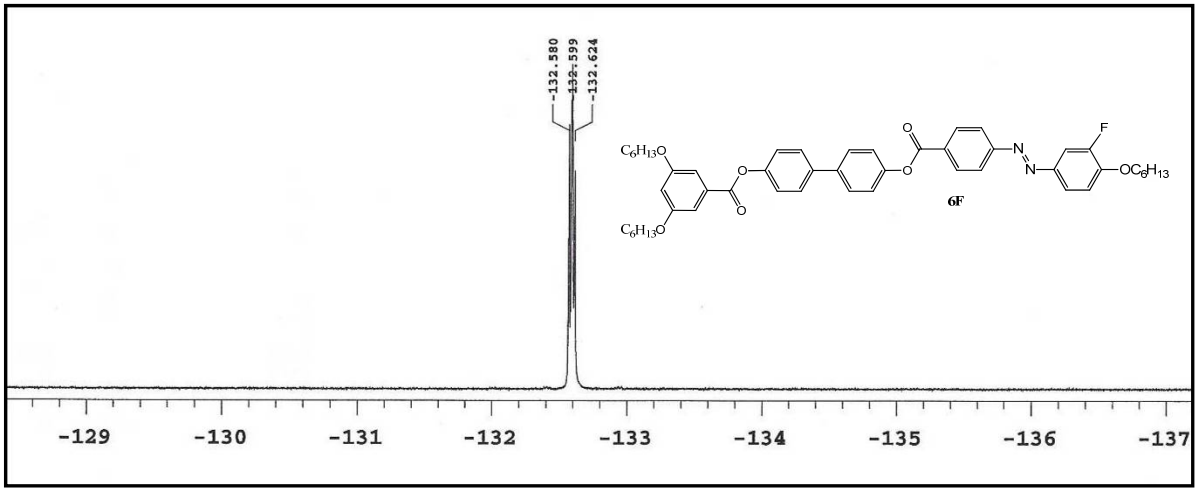

Figure S24. ^{19}F NMR Spectrum of **6F** (376 MHz, $CDCl_3$).

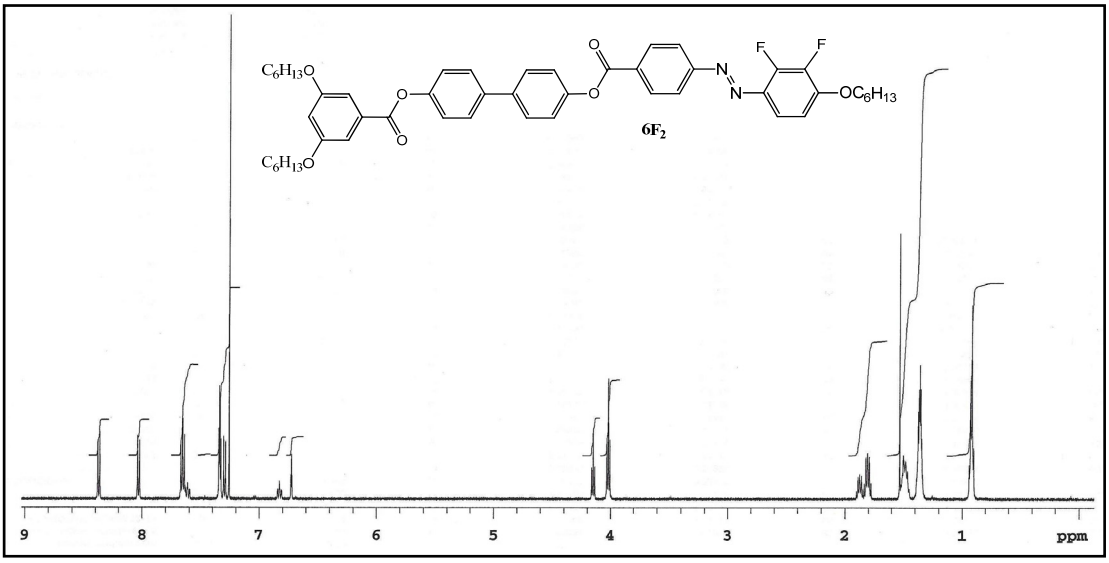

Figure S25. ^{1}H NMR Spectrum of **$6F_2$** (500 MHz, $CDCl_3$).

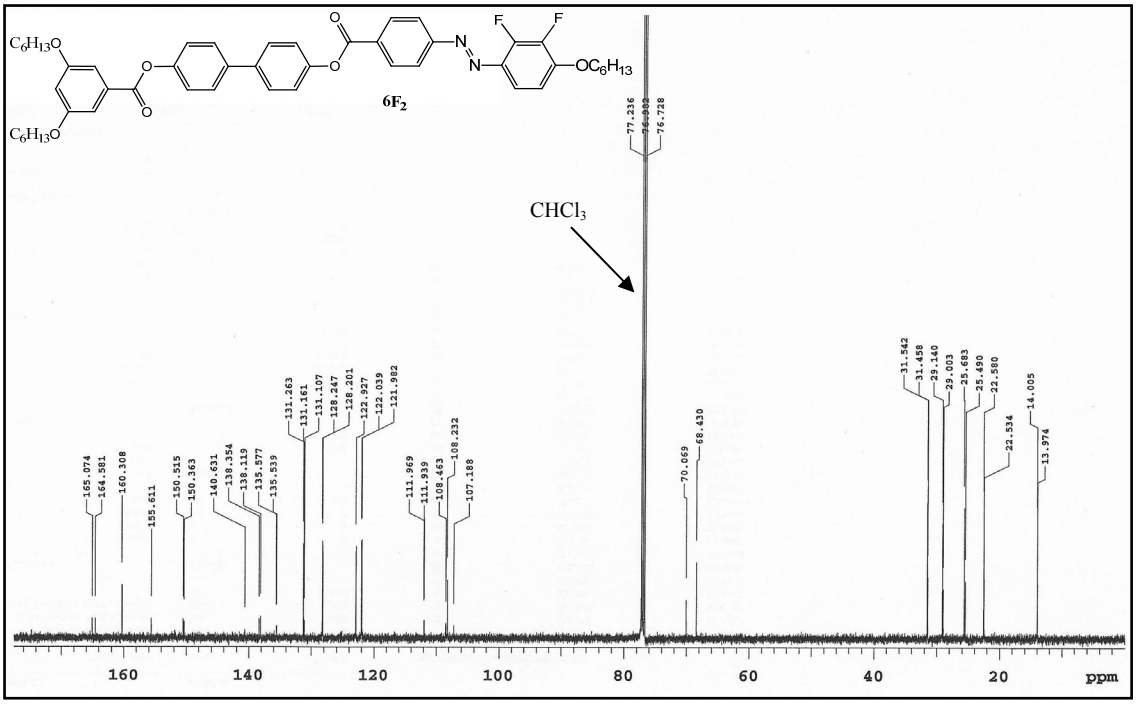

Figure S26. ^{13}C NMR Spectrum of **6F$_2$** (126 MHz, $CDCl_3$).

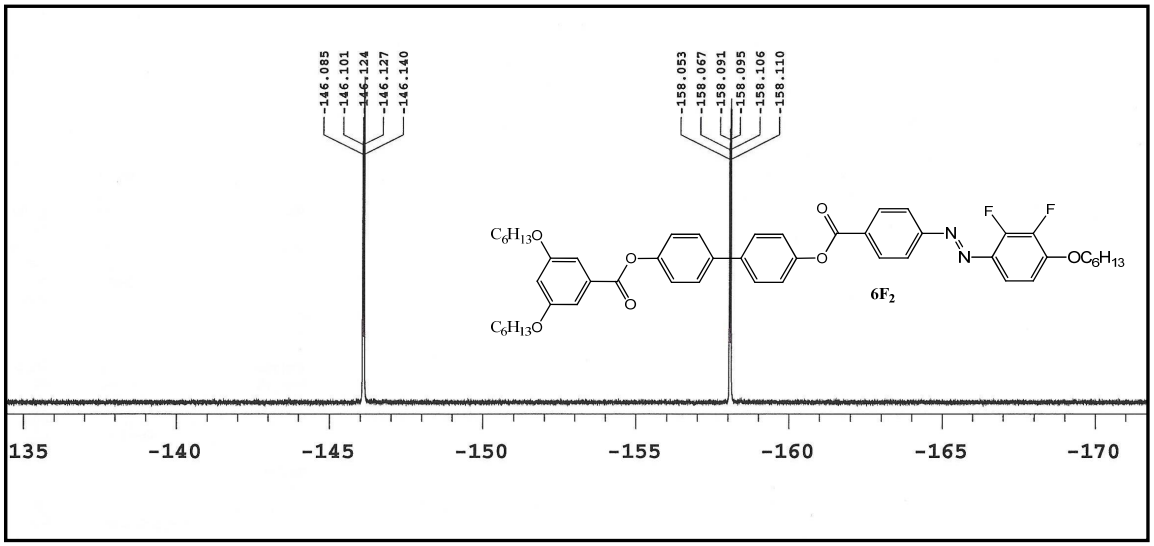

Figure S27. ^{19}F NMR Spectrum of **6F$_2$** (376 MHz, $CDCl_3$).

4. References

S1. M. Alaasar, S. Poppe, Q. Dong, F. Liu and C. Tschierske, *Angew. Chem. Int. Ed.*, 2017, **56**, 10801.

S2. M. Alaasar, M. Prehm and C. Tschierske, *Liq. Cryst.*, 2013, **40**, 656.

S3. M. Alaasar, M. Prehm, Y. Cao, F. Liu and C. Tschierske, *Angew. Chem. Int. Ed.*, 2016, **55**, 320.